Green Chemistry

PAPER

Cite this: *Green Chem.*, 2015, **17**, 1525

Core–shell Cu@(CuCo-alloy)/Al_2O_3 catalysts for the synthesis of higher alcohols from syngas†

Wa Gao,‡[a] Yufei Zhao,‡[b] Haoran Chen,[a] Hao Chen,[a] Yinwen Li,[a] Shan He,[a] Yingkui Zhang,[a] Min Wei,*[a] David G. Evans[a] and Xue Duan[a]

Received 22nd August 2014,
Accepted 5th December 2014

DOI: 10.1039/c4gc01633e

www.rsc.org/greenchem

The production of higher alcohols by the catalytic conversion of synthesis gas ($CO + H_2$) is one of the most promising approaches for the utilization of nonoil resources, in which bimetallic catalysts based on Cu and Fischer–Tropsch (FT) reaction active elements (*e.g.* Co, Fe, Ni) are efficient and cost-effective candidates. Herein, we demonstrate the fabrication of core–shell Cu@(CuCo-alloy) nanoparticles (NPs) embedded on a Al_2O_3 matrix *via* an *in situ* growth of CuCoAl-LDH nanoplatelets on aluminum substrates followed by a calcination–reduction process, and they serve as efficient catalysts toward CO hydrogenation to produce higher alcohols. The composition, particle size and shell thickness can be tuned by changing the Cu/Co molar ratio in the LDH precursors, and the best catalytic behavior was obtained over the Cu/Co (1/2) catalyst with a CO conversion of 21.5% and a selectivity (C_{6+} slate 1-alcohols) of 48.9%, which is superior to the traditional modified FT catalysts. XPS, *in situ* FTIR spectroscopy and HAADF-STEM revealed that the unique electronic and geometric interaction between Cu and Co in the Cu@(CuCo-alloy) NPs contributes to the significantly enhanced catalytic performances. In addition, the 3D hierarchical structure of the Cu@(CuCo-alloy)/Al_2O_3 catalyst facilitates mass diffusion/transportation as well as prevents hotspot formation, accounting for its stability and recyclability. The Cu@(CuCo-alloy)/Al_2O_3 catalyst with significantly improved catalytic behavior can be potentially used in CO hydrogenation to produce higher alcohols.

1. Introduction

Limited crude oil reserves and competition with the food industry associated with fermentation-based biofuel production inspire new efforts on effective catalytic transformation of alternative carbon sources to produce energy carriers and chemical feedstocks.[1] Production of higher alcohols by the catalytic conversion of synthesis gas ($CO + H_2$) derived from coal, natural gas, or renewable biomass is one of the most promising approaches for utilizing nonoil resources cleanly and efficiently.[1,2] Although Rh-based catalysts are effective for the formation of ethanol and other C_{2+} oxygenates from syngas, the very high cost of Rh prohibits its large scale utilization.[3] Recent research interest has been focused on the employment of nonprecious metal catalysts to produce higher alcohols from syngas over transition metal catalysts (*e.g.* Cu–Co, Cu–Fe systems),[4] but improvements in the overall catalytic activity, alcohol selectivity, and long-term stability of these materials are highly necessary.

Bimetallic catalysts, composed of two metal elements in either alloys or intermetallic compounds, emerge as a new material category with unique catalytic properties different from monometallic catalysts through modification of electronic and/or structural factors.[5] For the production of higher alcohols from syngas, bimetallic catalysts based on Cu and Fischer–Tropsch (FT) reaction active elements (*e.g.* Co, Fe, Ni) have been demonstrated as one of the most promising catalysts, in which Cu species assists in non-dissociative activation of CO for the CO insertion and subsequent alcohol formation while FT active elements act as active sites for dissociation of CO to form surface alkyl groups.[1a,2c,3,6] A synergistic effect between these two metal compositions is believed to be essential in this reaction.[1a,3,7] However, a phase separation of these bimetallic catalysts generally occurs during the reaction process, which would break the synergetic interaction and deteriorate the catalytic performance.[8] Moreover, the weak thermal conductivity of these powdered catalysts will induce hotspots and cause catalytic deactivation.[9] Therefore, the design and preparation of new bimetallic catalysts with desirable activity, selectivity and high

---

[a] *State Key Laboratory of Chemical Resource Engineering, Beijing University of Chemical Technology, Beijing, 100029, China. E-mail: weimin@mail.buct.edu.cn; Fax: +86-10-64425385; Tel: +86-10-64412131*

[b] *Photochemical Conversion and Optoelectronic Materials, Technical Institute of Physics and Chemistry, Chinese Academy of Sciences, Beijing, P. R. China*

† Electronic supplementary information (ESI) available. See DOI: 10.1039/c4gc01633e

‡ These authors contributed equally.

stability toward the production of higher alcohols from syngas remain a challenging goal.

Layered double hydroxides (LDHs) are a class of naturally occurring and synthetic materials generally expressed by the formula $[M^{2+}{}_{1-x}M^{3+}{}_{x}(OH)_2](A^{n-})_{x/n}\cdot mH_2O$.[10] The specialty of this material is that divalent and trivalent cations are uniformly distributed on the atomic scale in slabs of edge-sharing MO_6 octahedra that allow a close interaction between metal cations.[11] Recently, considerable interest has been focused on LDH materials as heterogeneous catalysts based on the versatility in their chemical composition and structural architecture.[12] In particular, a topotactic transformation of LDH materials to uniformly dispersed metal NPs supported on a metal-oxide support occurs upon calcination under a reductive atmosphere.[13] Inspired by the structural merits of LDH materials, we explored the idea of the incorporation of the Cu element and the FT reaction active Co element into the LDHs' precursor on the atomic scale, so as to fabricate supported CuCo bimetallic catalysts toward CO hydrogenation *via* the topotactic transformation process.

In this work, core–shell structure Cu@(CuCo-alloy) nanoparticles (NPs) embedded on the Al_2O_3 matrix with a high dispersion (denoted as Cu@(CuCo-alloy)/Al_2O_3) were fabricated *via* a facile two-step procedure, an *in situ* growth of CuCoAl-LDH nanoplatelets on aluminum substrates as the precursor followed by a calcination–reduction process (Scheme 1), and they serve as efficient catalysts toward the CO hydrogenation to produce higher alcohols. The HRTEM and HAADF-STEM results confirm that the well-dispersed core–shell structure Cu@(CuCo-alloy) NPs with a diameter of ∼15 nm were embedded on the Al_2O_3 matrix. The resulting materials demonstrate significantly improved catalytic CO hydrogenation to higher alcohols, and the best catalytic behavior was obtained over the Cu/Co (1/2) catalyst with a CO conversion of 21.5% and the C_{6+} slate 1-alcohol selectivity of 48.9%, which is superior to the traditional modified FT catalysts. The unique electronic and geometric interaction between Cu and Co in the Cu@(CuCo-alloy) NPs contributes to the significantly enhanced catalytic performance, and the bimetal phase separation is inhibited. In addition, the 3D hierarchical Cu@(CuCo-alloy)/Al_2O_3 catalyst facilitates mass diffusion and transportation, and the substrate prevents hotspot formation due to its high thermal conductivity. Therefore, our approach holds significant promise for the bimetallic CuCo core–shell structure as a new efficient catalyst toward the production of higher alcohols from syngas.

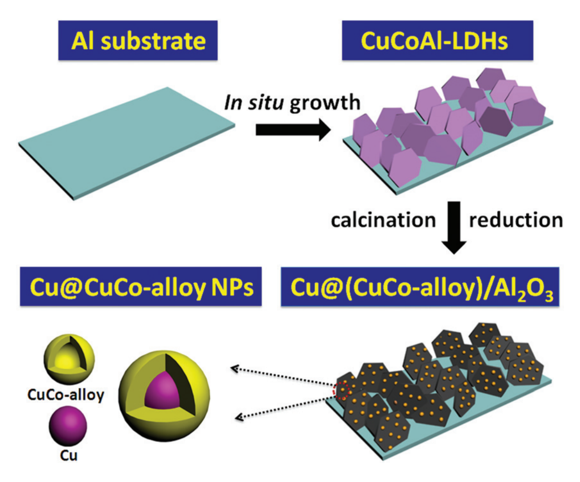

Scheme 1 Illustration of the structured Cu@(CuCo-alloy)/Al_2O_3 catalyst with a core–shell architecture derived from the CuCoAl-LDH film based on an *in situ* growth reaction followed by a calcination–reduction process.

2. Experimental section

2.1 Catalyst preparation

Preparation of the structured CuCoAl-LDH, CuAl-LDH, and CoAl-LDH films. CuCoAl-LDH, CuAl-LDH, and CoAl-LDH films as catalyst precursors were prepared by an *in situ* crystallization on an aluminum substrate.[14] The Al substrate was cleaned thoroughly with ethanol and deionized water in sequence.

In a typical procedure, 0.01 mol $Cu(NO_3)_2\cdot 3H_2O$ and $Co(NO_3)_2\cdot 6H_2O$ with a given molar ratio of Cu^{2+}/Co^{2+} (5/1, 2/1, 1/2, 1/5, respectively) and 0.06 mol NH_4NO_3 were dissolved in deionized H_2O (100 ml) to obtain a clear solution, which was adjusted to pH = 6.5 by adding diluted ammonia (1.5% NH_4OH). The Al substrate (15 cm × 20 cm) was placed vertically in the solution in an autoclave, which was placed in a conventional oven at 80 °C for 48 h. The substrate was then withdrawn from the autoclave, rinsed with ethanol, and dried at room temperature (denoted as CuCoAl-LDHs). The other CuAl-LDH and CoAl-LDH samples were prepared by a similar method with 0.01 mol of $Cu(NO_3)_2\cdot 3H_2O$ and $Co(NO_3)_2\cdot 6H_2O$, respectively.

Preparation of the structured Cu@(CuCo-alloy)/Al_2O_3, Cu/Al_2O_3, and Co/Al_2O_3 catalysts. The CuCoAl-LDH, CuAl-LDH, and CoAl-LDH precursor films were calcined in air at 500 °C for 5 h with a heating rate of 2 °C min^{-1} to obtain the mixed metal oxides (denoted as CuCoAl-MMO, CuAl-MMO, and CoAl-MMO). Subsequently, the three samples were reduced under a hydrogen atmosphere at 500 °C for 5 h with a heating rate of 2 °C min^{-1}. The final catalysts were labeled as Cu@(CuCo-alloy)/Al_2O_3, Cu/Al_2O_3, and Co/Al_2O_3.

Preparation of the powdered CuCo/Al_2O_3 catalyst. The powdered CuCo/Al_2O_3 as a reference catalyst was prepared by a conventional impregnation method, in which the metal contents of Cu and Co were controlled to be 20 wt% and 42 wt%, respectively (see details in the ESI†), in accordance with those of the optimal catalyst Cu@(CuCo-alloy)/Al_2O_3 (Cu/Co = 1/2). In a typical procedure, commercial γ-Al_2O_3 was used as the support. An aqueous solution of $Cu(NO_3)_2\cdot 3H_2O$ and $Co(NO_3)_2\cdot 6H_2O$ was added dropwise into the alumina support with continuous stirring, followed by aging at room temperature for 4 h. After the impregnation, the sample was calcined in air at 100 °C for 2 h and then at 500 °C for 5 h (heating rate: 2 °C min^{-1}). After hydrogen reduction at 500 °C for 5 h with a heating rate of 2 °C min^{-1}, the final catalyst was labeled as powdered-CuCo/Al_2O_3.

2.2 Characterization of samples

The X-ray diffraction (XRD) patterns of samples were obtained on a Shimadzu XRD-6000 diffractometer, using Cu Kα radiation (λ = 0.154 nm) at 40 kV, 30 mA, a scanning rate of 5° min^{-1}, a step size of 0.02° s^{-1}, and a 2θ angle ranging from 3 to 70°. Elemental analysis for Cu and Co was performed using a Shimadzu ICPS-75000 inductively coupled plasma emission spectrometer (ICP-ES). The sample morphology was investigated using a scanning electron microscope (SEM; Zeiss Supra 55) with an accelerating voltage of 20 kV, combined with energy dispersive X-ray spectroscopy (EDX) for the determination of the metal composition. Transmission electron microscopy (TEM) was performed using a Hitachi H-800 transmission electron microscope operated at 100 kV. High resolution transmission electron microscopy (HRTEM) was carried out on a JEM-3010 at an accelerating voltage of 200 kV. Surface elemental analysis was performed using an ESCALAB250 X-ray photoelectron spectroscope (XPS) equipped with Mg Kα radiation. The C 1s peak at 284.6 eV was used as a calibration peak. The modified Auger parameter (α') is defined as

$$\alpha' = E_b + E_k \tag{1}$$

where E_b and E_k are the binding and kinetic energies of the dominant core electron and Auger electron line for a particular element, respectively.[15]

Temperature-programmed reduction (TPR) was conducted on a Micrometric ChemiSorb 2750 chemisorption instrument with a thermal conductivity detector (TCD). About 100 mg of samples were loaded in a quartz reactor. TPR was carried out with a heating ramp rate of 5 °C min^{-1} in a stream of 10% H_2 in Ar to a sample temperature of 800 °C, with a total flow rate of 25 ml min^{-1}.

In situ Fourier-transformed infrared absorption (FTIR) spectroscopy of CO was carried out in a quartz cell equipped with KBr windows allowing sample activation and successive measurements in the range of 25–600 °C, at a pressure as low as 10^{-4}. About 50 mg of the sample was pressed into a disk and activated in the same cell which is used for the measurement. The thermal treatment was performed either under dynamic vacuum or under static conditions, according to procedures discussed below. FTIR spectra were recorded with a Nicolet 380 instrument spectrophotometer at a spectrum resolution of 4 cm^{-1} and an accumulation of 64 sans. After nitrogen pre-treatment at 200 °C for 60 min and hydrogenation treatment at 500 °C for 60 min, the sample was scanned to get a background record below a pressure of 2×10^{-4} Pa. Subsequently, the sample was exposed to a CO flow at 30 °C for another 120 min. Sample scanning for the adsorbed CO on the studied sample was conducted after the pressure was reduced below 2×10^{-4} Pa again.

2.3 Catalytic evaluation

Carbon monoxide hydrogenation reaction was carried out in a fixed bed stainless steel tubular microreactor (8 mm in diameter, 500 mm in length). The structured catalyst was rolled and placed vertically in the stainless steel tubular microreactor. The total Cu@(CuCo-alloy)/Al_2O_3 catalyst on the Al substrate was ~1.2 g. The temperature of the reactor was controlled *via* a temperature controller. H_2, CO and N_2 were purged into the reactor at a desired rate by mass flow controllers. Nitrogen was used as an internal standard gas in the reactor feed. Prior to the reaction, the catalyst was reduced *in situ* in a flow of H_2 (40 ml min^{-1}) under atmospheric pressure at 500 °C for 5 h. The reactor was cooled down to 220 °C and synthesis gas with a flow rate of 40 ml min^{-1} (H_2: CO = 2.0, v/v) was introduced to increase the pressure to 2.0 MPa. During the process, the total pressure in the system was kept at 2.0 MPa (H_2/CO = 2.0, v/v) with a space velocity of 2000 ml g_{cat}^{-1} h^{-1}. The outlet gas components (CO, H_2, CH_4, CO_2 and N_2) were determined using an online GC-2014C Shimadzu gas chromatograph with a TCD detector (TDX-1 column). The liquid alcohol and hydrocarbon products were captured using an ice-water bath and analyzed off-line with the same chromatograph (a PEG-20 M capillary column and a FID detector Porapak Q column).

3. Results and discussion

3.1 Structural and morphological study of the catalysts

Fig. 1A shows the XRD patterns of the CuCoAl-LDH film (Cu/Co = 1/2) obtained by the *in situ* growth method on the Al substrate as well as the corresponding powdered sample scraped from the substrate for comparison. For the CuCoAl-LDH film (curve a), a weak reflection was observed at 2θ 35.1°, which can be attributed to the [012] reflection of the LDH phase; the strong reflection appears to originate from the Al sub-

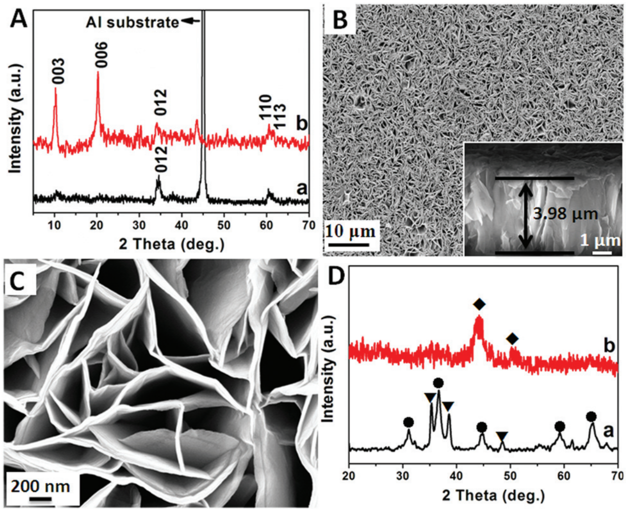

Fig. 1 (A) XRD patterns of (a) the as-prepared CuCoAl-LDH (Cu/Co = 1/2) film, (b) the corresponding powdered material scraped from the film. (B and C) SEM images of the as-prepared CuCoAl-LDH film (the film thickness is shown in the inset of B). (D) XRD patterns of (a) CuCoAl-MMO, (b) the final reduction sample. Crystalline phase: (●) Co_3O_4, (▼) CuO, (◆) CuCo.

strate.[13,16] The XRD pattern of the powdered material scraped from the LDH film (curve b) shows a series of reflections at 2θ 11.7°, 23.5°, 35.1°, 61.0° and 62.5°, corresponding to the [003], [006], [012], [110] and [113] reflection of an LDH phase, respectively, which demonstrates the formation of a CuCoAl-LDH film on the Al substrate.[11] The morphology of the LDH film revealed by SEM is shown in Fig. 1B and C. Top-view and side-view of the LDH film show uniform hexagonal plate-like microcrystals with a diameter of ~4 μm and a thickness of 10–20 nm, whose *ab*-plane is perpendicular to the substrate. This is consistent with the XRD results in Fig. 1A. Calcination of the LDH precursor leads to its transformation to mixed metal oxides (CuCoAl-MMO) (Fig. 1D, curve a), in which a CuO crystalline phase (JCPDS 89-5899) and a Co_3O_4 phase (JCPDS 78-1970) are identified in the XRD pattern. The final structured Cu@(CuCo-alloy)/Al_2O_3 catalyst was subsequently obtained *via* a reduction process of CuCoAl-MMO (see Scheme 1). As shown in Fig. 1D (curve b), a broad reflection at 2θ 44.1° is observed, which can be attributed to the superimposition of the Cu(111) and Co(111) reflection. This indicates the formation of the CuCo alloy to some extent during the reduction process. According to the phase diagram of binary Co–Cu, only a maximum of 9 at% Cu can be dissolved in the Co metal.[17] Therefore, the metal Cu, Co and CuCo alloy may coexist in the final structured sample, which will be further discussed in the next section.

The architectural feature of the final reduction sample was revealed by SEM (Fig. 2A), in which the sample inherits the original flake morphology of the LDH precursor, and no agglomeration or sintering of adjacent nanoflakes were observed. Notably, numerous well-dispersed NPs with a rather high density on the Al_2O_3 matrix are observed in Fig. 2B and C. The high-angle annular dark field microscopy (HAADF--STEM) and the corresponding energy-dispersive spectroscopy (EDS) mapping demonstrate that both Cu and Co elements have a uniform and homogeneous distribution (Fig. 2D). The detailed structural feature of the obtained well-dispersed NPs was further revealed by HRTEM and HAADF-STEM. The HRTEM image (Fig. 3B) of a nanoflake reveals that the NPs (15–20 nm in diameter) possess a core–shell structure, in which a round core and an uneven shell (thickness: 2.4–3.5 nm) can be recognized. According to the lattice distance of 0.209 nm, the core is determined to be metal Cu (Fig. 3C).[18] However, the shell is not uniform; several interconnected parts with different lattice spacings (*e.g.* 0.206, 0.252, or 0.302 nm) are identified, which can be assigned to the CuCo alloy phase and some tiny CoO phase.[19] This suggests that in the bimetallic CuCo sample, metal Cu exists in the core section while a CuCo alloy phase accompanied by a tiny CoO phase is located in the exterior shell. To gain further insights into the structure of the core–shell NPs, EDS analysis was applied to characterize the structure and composition of a typical NP. The analysis depth of EDS is 0.5–3.0 μm, so the whole Cu@(CuCo-alloy) nanoparticle can be detected. As shown in Fig. 3D, the Cu signal is mainly detected in the central zone, while both Cu and Co signals are observed in the shell (Fig. 3D, inset). The results provide a striking demonstration of the core–shell structure: the metal Cu in the core and both the elements in the Co-dominated outer shell. This suggests that CuO is firstly reduced to metallic Cu nanoparticles during the reduction process of CuCoAl-MMO (see Fig. 8), which serves as the core for the further reduction of Co_3O_4 to

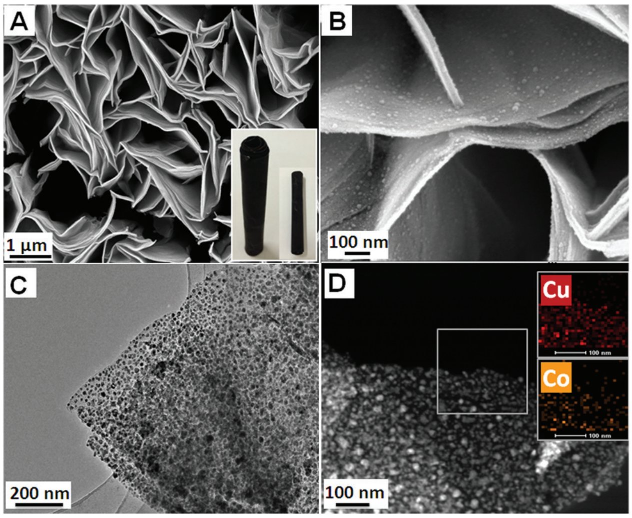

Fig. 2 (A and B) SEM images of the Cu@(CuCo-alloy)/Al_2O_3 sample (Cu/Co = 1/2); the inset in (A) shows the photograph of the rolled Cu@(CuCo-alloy)/Al_2O_3 film catalyst. (C) TEM image of the Cu@(CuCo-alloy)/Al_2O_3 sample. (D) HAADF-STEM image of the Cu@(CuCo-alloy) NPs dispersed on the Al_2O_3 matrix with the Cu and Co EDS mapping (inset).

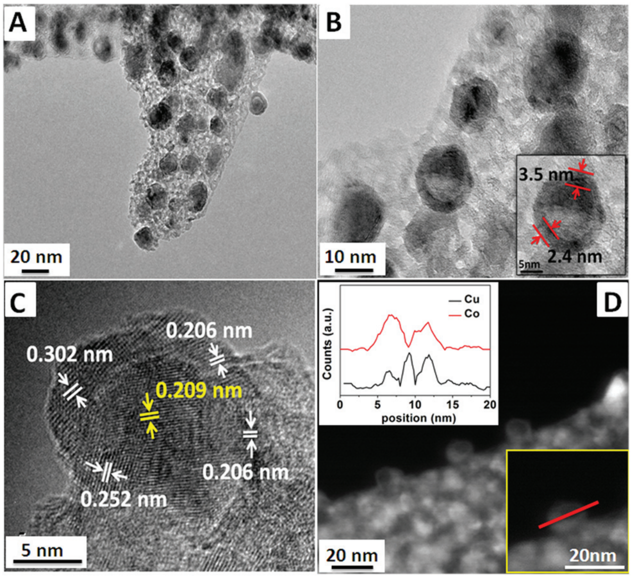

Fig. 3 Structural features of the Cu@(CuCo-alloy)/Al_2O_3 (Cu/Co = 1/2) sample: (A) a low magnification TEM; (B) a high magnification TEM; (C) HRTEM of a single Cu@(CuCo-alloy) NP; (D) HAADF-STEM for a single Cu@(CuCo-alloy) NP with the EDS line scan profile along the pink line: the black and red lines are the EDS line spectra of Cu–K and Co–K, respectively.

metallic Co. Meanwhile, partial Cu atoms migrate to the surface to form the CuCo-alloy shell, due to the relatively lower surface energy of Cu compared with Co (1.9 J m^{-2} *vs.* 2.7 J m^{-2}).[17] It has been discussed above that for the Cu–Co bimetallic system, only a maximum of 9 at% Cu can be dissolved in the Co metal to form the CuCo alloy. Therefore, the formation of a core–shell structure (Cu as the core and CuCo alloy as the shell) would facilitate a maximum CuCo alloy. Moreover, this specific structure improves the unique electronic and geometric interaction between Cu and Co species and effectively avoids phase separation in the catalytic reaction, which will be discussed in the next section. In contrast, no obvious core–shell structure is observed for the powdered-CuCo/Al_2O_3 sample (Fig. S1B and S1C†). Separate Cu, CoO and Co_3O_4 phases are observed, implying that a phase separation occurs during the reduction process. The results indicate that a uniform distribution of metal elements in the LDH precursor is necessary for the growth of the Cu nanoparticle core and the subsequent CuCo-alloy shell in the Cu@(CuCo-alloy)/Al_2O_3 catalyst. This is successfully demonstrated by the LDH precursor approach while it cannot be achieved by the conventional impregnation method.

3.2 The evaluation of the catalytic performance

The catalytic performance of the structured Cu@(CuCo-alloy)/Al_2O_3 (Cu/Co = 1/2) catalyst was studied in comparison with that of the powdered-CuCo/Al_2O_3 (Cu/Co = 1/2) catalyst. As shown in Fig. 4, both catalysts are active in 1-alcohol synthesis, and the total 1-alcohol selectivity (S_{ROH}) increases upon decreasing the reaction temperature. A S_{ROH} value of 50.6% is obtained for the Cu@(CuCo-alloy)/Al_2O_3 catalyst at 220 °C, while the maximum S_{ROH} value is only 33.1% for the powdered-CuCo/Al_2O_3 catalyst. In addition, the C_{6+} slate 1-alcohol selectivity in the total 1-alcohol distribution for Cu@(CuCo-alloy)/Al_2O_3 at 220 °C reaches approximately 48.9%, which is higher than that of the powdered-CuCo/Al_2O_3 (Cu/Co = 1/2) (38.7%). Moreover, it should be noted that CO_2 production is unwanted but frequently reported to be difficult to exclude.[20] As the CO conversion rate increases, an increase of CO_2 production is frequently related to the occurrence of the water-gas shift reaction, $CO + H_2O \rightarrow CO_2 + H_2$. In this work, for Cu@(CuCo-alloy)/Al_2O_3, the increase of the CO conversion from 200 to 260 °C does not entail a drastic change in the CO_2 production, while predominant CO_2 is produced over the powdered-CuCo/Al_2O_3 (Cu/Co = 1/2) catalyst in the same temperature range. The most intriguing observation in Fig. 4 is the high α-chain-lengthening probability of 1-alcohol formation for the Cu@(CuCo-alloy)/Al_2O_3 catalyst. The α-value ranges from 0.79 to 0.62 at a reaction temperature between 200 and 280 °C, which therefore achieves the purpose of maximizing the yields of C_{6+} slate 1-alcohols. However, the powdered-CuCo/Al_2O_3 (Cu/Co = 1/2) catalyst fails to produce C_{6+} slate 1-alcohols (Fig. 4 and Table 1), with the α-value ranging from 0.68 to 0.40 at the same reaction temperature. The results indicate that the Cu@(CuCo-alloy)/Al_2O_3 with a unique core–shell structure derived from the LDH precursor exhibits significantly enhanced catalytic behavior.

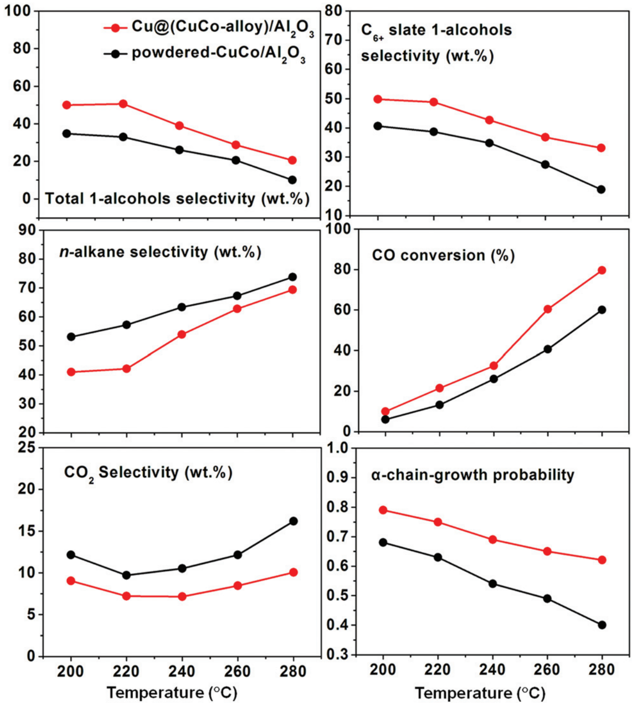

Fig. 4 Catalytic performances of Cu@(CuCo-alloy)/Al_2O_3 (Cu/Co = 1/2) and powdered-CuCo/Al_2O_3 (Cu/Co = 1/2) catalysts, respectively. Temp. = 220 °C, *P* = 2 MPa, GHSV = 2000 ml g_{cat}^{-1} h^{-1}, H_2/CO = 2.0. The α-chain-growth probability is calculated according to $\ln(W_n/n) = n\ln a + \ln(1-\alpha)^2/\alpha$, in which *n* is the number of carbon atoms in 1-alcohol and W_n is the weight fraction of 1-alcohol that contains *n* carbon atoms.

It is well-known that Cu is the major element for methanol synthesis, serving in the dissociative chemisorption of hydrogen and the associative adsorption of CO, while Co affords the active site of FT function of dissociative CO adsorption (C–C chain growth) and hydrogenation.[1a,3,7] Accordingly, the synergetic effect of Cu and Co plays a key role in determining the catalytic performance. Therefore, a detailed catalytic performance study of this binary system was performed by changing the relative amount of Cu and Co. As shown in Table 1, the selectivity patterns of various Cu@(CuCo-alloy)/Al_2O_3 catalysts change accordingly. The monometallic Co/Al_2O_3 catalyst exhibits the highest activity in Fischer–Tropsch synthesis producing mostly 95.1% of hydrocarbons with only a trace of alcohols (2.6%), while methanol (98.9%) is the major reaction product with the lowest selectivity of hydrocarbons for the monometallic Cu/Al_2O_3 catalyst. All the CuCo bimetallic catalysts are selective between alcohols and hydrocarbons at 220 °C, *i.e.* with the increase of Cu/Co ratio, the alcohol selectivity increases while the hydrocarbon selectivity decreases gradually. However, the selectivity of C_{6+} slate 1-alcohols ($S_{\mathrm{C6+OH}}$) shows a primary enhancement followed by a sharp decline, and the highest $S_{\mathrm{C6+OH}}$ value of 48.9% present in the sample of Cu/Co (1/2), with the S_{ROH} value of 50.6% and the S_{CO2} value of 7.2%. To sum up, a distinct difference in the

Table 1 Catalytic performances of Cu@(CuCo-alloy)/Al_2O_3 catalysts with various Cu/Co ratios and the powdered-CuCo/Al_2O_3 (Cu/Co = 1/2) catalyst toward the synthesis of higher alcohols[a]

		Carbon selectivity (C mol%)[b]			Alcohol selectivity (wt%)[c]			
Catalyst	CO conv. (%)	CO_2	ROH	HC	MeOH	EtOH	$C_{3-5}OH$	$C_{6+}OH$
Co/Al_2O_3	36.6	2.3	2.6	95.1	2.3	2.6	27.1	68.0
Cu/Co (1/5)	32.9	4.7	36.2	59.1	15.1	16.8	18.5	49.6
Cu/Co (1/2)	21.5	7.2	50.6	42.2	19.2	16.5	15.4	48.9
Cu/Co (2/1)	20.7	7.9	52.5	39.6	20.9	17.6	22.3	39.2
Cu/Co (5/1)	21.9	8.6	66.8	24.6	66.7	10.3	9.2	13.8
Cu/Al_2O_3	22.3	9.5	86.7	3.8	98.9	0.6	0.3	0.2
Powdered-CuCo/Al_2O_3 (1/2)	13.1	9.8	22.9	67.3	22.6	19.8	18.9	38.7

[a] Reaction conditions: Temp. = 220 °C, P = 2 MPa, $R(H_2/CO)$ = 2, GHSV = 2000 ml g_{cat}^{-1} h^{-1}. [b] Carbon selectivity is defined as the selectivity of all the carbon-containing products from converted carbon, and the values are recalculated from the original data; HC = total hydrocarbons including methane; ROH = total alcohol including methanol. [c] Alcohol distribution (wt%): the proportion of each alcohol in the total value.

performances of these bimetal samples is observed, suggesting a strong copper–cobalt interaction which is responsible for the catalytic selectivity.

Time-on-stream analysis of the best-performing Cu@(CuCo-alloy)/Al_2O_3 (Cu/Co = 1/2) catalyst was investigated at 220 °C with a relative pressure of 2 MPa for up to 48 h as shown in Fig. 5. The catalyst selectivity decreases to a slight extent during the initial 10 h and then maintains at a constant value (43%). This stable activity can be ascribed to the specific core–shell structure of Cu@(CuCo-alloy) NPs in which a unique electronic and geometric interaction between Cu and Co species suppresses the phase separation; the grafting of active NPs onto the Al_2O_3 matrix guarantees a satisfactory stability. Furthermore, the 3D hierarchical Cu@(CuCo-alloy)/Al_2O_3 catalyst provides open tunnels, facilitating mass diffusion and transportation. HRTEM images of the used Cu@(CuCo-alloy)/Al_2O_3 catalyst are shown in Fig. S2,† in which no obvious aggregation is observed and the bimetallic CuCo NPs maintain the core–shell structure with a mean size of 30 nm. In the case of the used powdered-CuCo/Al_2O_3 (Cu/Co = 1/2) catalyst however, an increase in the mean size (42 nm) of bimetallic CuCo NPs was observed (Fig. S3†).

3.3 Correlation studies on the structure and catalytic behavior

The results above clearly show that the Cu@(CuCo-alloy)/Al_2O_3 catalysts with a core–shell structure display excellent catalytic behavior. To gain an understanding of the structure–performance relationship, XRD, TPR, XPS and FTIR measurements were performed to elucidate the electronic and geometric structure of these bimetal catalysts. The nominal and determined metal ratios of the products by inductively coupled plasma emission spectrometer (ICP-ES) are also summarized in Table S1.† Fig. 6 shows the XRD patterns of the Cu@(CuCo-alloy)/Al_2O_3 catalysts with various Cu/Co ratios. For the Cu/Co (5/1) sample, the Cu(111) and Co(111) reflections are observed at 2θ 43.3° and 44.3°, respectively, suggesting a separate Cu and Co phase without the formation of a significant degree of solid solution. With the decrease of Cu/Co ratio, the reflections of Cu and Co metals gradually combine together. The Cu/Co (1/5) sample exhibits a single reflection located between metallic Cu (2θ [111] = 43.3°) and Co (2θ [111] = 44.3°), which implies that Cu atoms are completely incorporated into the Co

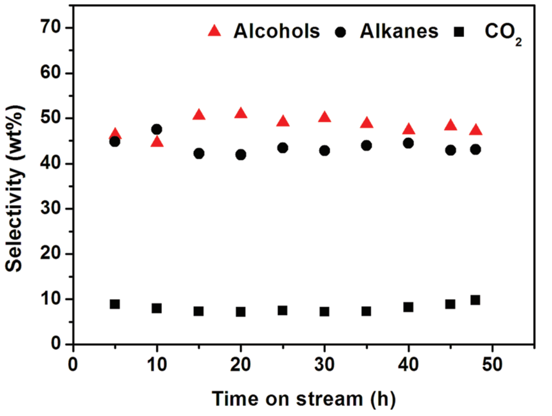

Fig. 5 Product selectivities as a function of time on stream over the Cu@(CuCo-alloy)/Al_2O_3 catalyst (Co/Cu = 1/2) performed at 220 °C, 2 MPa and H_2/CO = 2.

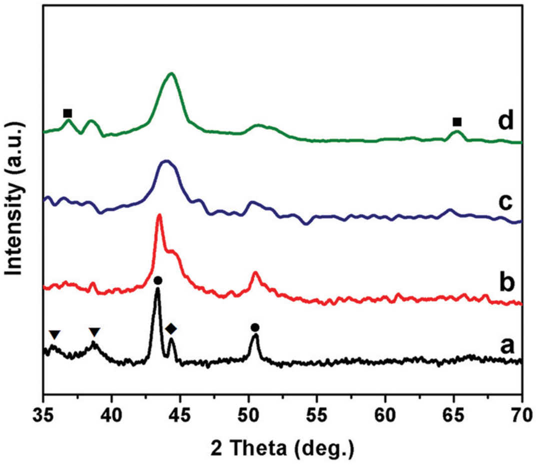

Fig. 6 XRD patterns of Cu@(CuCo-alloy)/Al_2O_3 catalysts with various Cu/Co ratios: (a) Cu/Co = 5/1, (b) Cu/Co = 2/1, (c) Cu/Co = 1/2, (d) Cu/Co = 1/5. Crystalline phase: (●) Cu, (◆) Co, (▼) CuO, (■) Co_3O_4.

lattice in the formation of the CuCo alloy phase. This result indicates that the degree of alloying can be tuned by changing the Cu/Co ratio in the CuCoAl-LDH precursor, and a lower Cu/Co ratio facilitates the formation of the CuCo alloy. The XRD pattern of the used Cu@(CuCo-alloy)/Al_2O_3 (Co/Cu = 1/2) catalyst shows that the CuCo alloy phase is stable after the reaction (Fig. S4†). As shown in Fig. 7, the Cu NPs in the Cu/Al_2O_3 sample show a particle size of 13.2 nm (Fig. 7A). With the decrease of Cu/Co ratio in the bimetal catalysts, both the particle size and the shell thickness of Cu@(CuCo-alloy) NPs increase in the following order: Cu/Co (2/1) < Cu/Co (1/2) < Cu/Co (1/5) (Fig. 7B–D). The average size of Cu@(CuCo-alloy) NPs was calculated to be ~9.2, 13.9, and 18.1 nm for Cu/Co (2/1), Cu/Co (1/2), and Cu/Co (1/5), with the thickness of ~1.8, 4.1, and 6.2 nm, respectively. In brief, the core–shell structure Cu@(CuCo-alloy)/Al_2O_3 catalysts with various particle sizes and shell thicknesses can be obtained by controlling the Cu/Co ratio in CuCoAl-LDH precursors. The alloying degree and shell thickness will influence the surface composition of catalytic active sites, which will be further studied by the following investigations.

The H_2-TPR measurements were conducted to investigate the reducibility and the synergistic effect of Cu–Co in Cu@(CuCo-alloy)/Al_2O_3 samples and the corresponding profiles are shown in Fig. 8. The sample of CuAl-MMO (Fig. 8, curve a) exhibits a main peak at 193 °C, which is attributed to the reduction of CuO to metal Cu,[21] while the sample of CoAl-MMO (Fig. 8, curve e) displays two peaks at 371 °C and 568 °C, assigned to the reduction of Co_3O_4 in two steps (Co_3O_4/CoO/Co).[22] In the case of CuCoAl-MMO samples (Fig. 8, curves b–d), both the reduction of CuO (in the low temperature range) and Co_3O_4 (in the high temperature range) are observed. Obviously, compared with the CoAl-MMO sample, the broad hydrogen consumption peak for the reduction of Co_3O_4 shifts to a lower temperature (from 568 °C to 359 °C) along with the increase of the Cu content (from Cu/Co = 0/1 to Cu/Co = 5/1), indicating a Cu-promoted reduction of Co species to produce the CuCo alloy.[23] However, the H_2 consumption peak of the CuO phase shifts gradually to a higher temperature (from 193 °C to 279 °C) along with the increase of the Co content (from Cu/Co = 1/0 to Cu/Co = 1/2). The results suggest that a strong synergistic effect between copper and cobalt occurs in the reduction process of CuCoAl-MMO samples.[22,24]

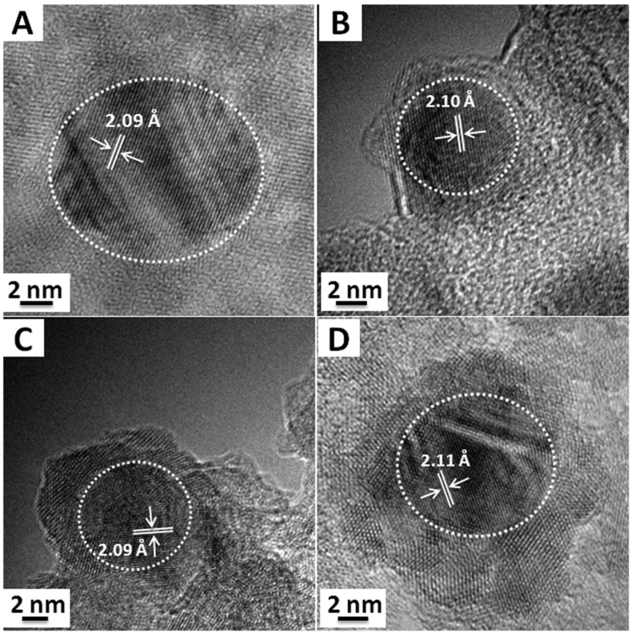

Fig. 7 HRTEM images of the Cu/Al_2O_3 and Cu@(CuCo-alloy)/Al_2O_3 samples with various Cu/Co ratios: (A) Cu/Al_2O_3, (B) Cu/Co = 2/1, (C) Cu/Co = 1/2, and (D) Cu/Co = 1/5.

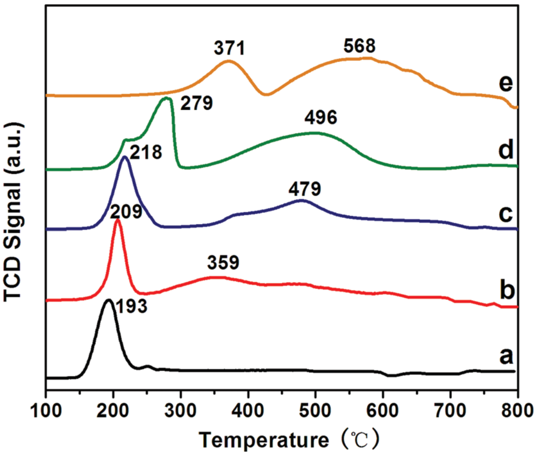

Fig. 8 H_2-TPR profiles of CuAl-MMO, CoAl-MMO and CuCoAl-MMO samples with various Cu/Co ratios: (a) CuAl-MMO, (b) Cu/Co = 5/1, (c) Cu/Co = 2/1, (d) Cu/Co = 1/2 and (e) CoAl-MMO.

To further confirm the formation of the core–shell structure and the active site state of the Cu@(CuCo-alloy)/Al_2O_3 catalyst, XPS measurements were performed. For all the samples, two peaks (Fig. 9A) centered at ~931.9 and 951.5 eV are mainly ascribed to Cu $2p_{3/2}$ and Cu $2p_{1/2}$ peaks of Cu^0 and/or Cu^+, respectively, which makes it difficult to differentiate these two species based on their Cu 2p binding energies.[24] Therefore, the modified Auger parameter (α') was used to distinguish Cu^0

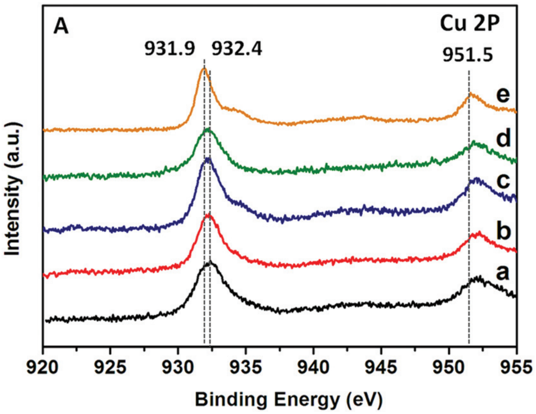

Fig. 9 Cu XPS spectra of Cu/Al_2O_3 and Cu@(CuCo-alloy)/Al_2O_3 samples with various Cu/Co ratios: (a) Cu/Co = 1/5, (b) Cu/Co = 1/2, (c) Cu/Co = 2/1, (d) Cu/Co = 5/1, and (e) Cu/Al_2O_3.

from Cu^+ species, which is an important energy parameter for identifying the chemical state of elements where the chemical shift is very small or comparable to the energy resolution of the instrument.[15] As shown in Table S2,† the modified Auger parameter for the Cu@(CuCo-alloy)/Al_2O_3 samples with various Cu/Co ratios is close to the reported value for Cu^0 (~1851.3 eV).[25] For the used Cu@(CuCo-alloy)/Al_2O_3 (Co/Cu = 1/2) catalyst (Fig. S6†), the Cu LMM XAES spectrum shows an Auger peak of Cu^+ (~915.6 eV) besides that of Cu^0.[26] However, the modified Auger parameter is ~1851.2 eV, indicating that only a slight Cu^0 species is oxidized during the reaction process.[25] For the Co 2p XPS spectra of the fresh and used Cu@(CuCo-alloy)/Al_2O_3 catalyst (Fig. 10 and S8†), a broad peak in the range 775–785 eV is observed, which is difficult to determine the chemical state of Co species.[27] However, the modified Auger parameter for these samples ranges from 1550.9 to 1552.2 eV (Table S2†), close to the reported value for Co^0 (~1551.2 eV) rather than Co^{2+} (~1553.8 eV).[28] This indicates that Co^0 is the predominant species both in the fresh and used Cu@(CuCo-alloy)/Al_2O_3 catalyst and the structure of the CuCo alloy shell remains stable during the reaction process. As listed in Table 2, the Cu/Co ratio at the surface (2.88/1.00) is much smaller than the bulk ratio for the Cu/Co (4.81/1.00) sample, indicating the existence of the predominant Co metal in the shell section. Notably, the surface Cu/Co ratio is bigger than the bulk ratio for the Cu/Co (2/1) sample, which is indicative of the migration of copper atoms to the crystalline surface to form a CuCo alloy shell. It is therefore reasonable to conclude that the reduced bimetal NPs possess a core–shell structure, with predominant Cu in the core and the CuCo alloy in the outer shell. Furthermore, it is worth noting that the Cu $2p_{3/2}$ peak shifts from 931.9 (Cu-only) to 932.4 eV upon alloying with increased Co (Cu/Co = 1/5) (Fig. 9, from curves e to a), while a shift from 780.9 (Co-only) to 780.0 eV (Cu/Co = 2/1) can be observed for the Co $2p_{3/2}$ peak (Fig. 10, from curves a–d). An upshift of Co $2p_{3/2}$ is not observed for the Cu/Co (5/1) sample (Fig. 10, curve e), probably due to a portion of the unalloyed Co. This indicates the diminishing electron density in the Cu^0 nucleus, resulting from the electron scavenging property of Co^0.[29] Therefore, a strong electron interaction between Cu and Co occurs on the catalyst surface, wherein electrons likely transfer from Cu species to Co species in the bimetal Cu@(CuCo-alloy)/Al_2O_3 catalyst.

In situ FTIR is a useful surface-sensitive technique to study the adsorption behavior of catalysts under reaction conditions and to elucidate the nature of the active sites and the surface intermediates involved in the reaction. Fig. 11 displays IR spectra of CO adsorbed on Co/Al_2O_3 and Cu@(CuCo-alloy)/Al_2O_3 samples with different Cu/Co ratios (5/1, 2/1, 1/2, 1/5). The IR spectra of Co/Al_2O_3, bimetallic Cu/Co (1/5) and Cu/Co (1/2) catalysts (with predominant Co) exhibit strong bands with a maximum at 1991, 1980, and 1959 cm^{-1}, respectively, which can be assigned to the bridge-type adsorbed CO on Co metal sites.[30] In comparison with the monometallic Co/Al_2O_3 catalyst (1991 cm^{-1}), the significant shifting of this peak to lower frequencies (from 1991 to 1959 cm^{-1}) for the bimetallic samples along with the increase of the Cu content indicates that the surface Co species is slightly negatively charged.[29b] That is, electron transfer from surface Cu species to Co species occurs, as also supported by the XPS data discussed above. Upon further increasing the Cu content (Cu/Co = 2/1 sample: Fig. 11, curve d), the bridge-type adsorbed CO disappears completely, while the linearly adsorbed CO on the Co metal is observed. The peak fitting of the band observed in this region reveals the presence of two different peaks (2015 and 2038 cm^{-1}), which point to different Co^0 sites. The Co-carbonyl

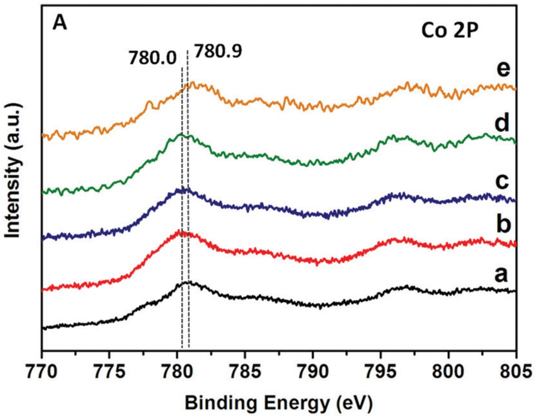

Fig. 10 Co XPS spectra of (a) Co/Al_2O_3 and Cu@(CuCo-alloy)/Al_2O_3 samples with various Cu/Co ratios: (b) Cu/Co = 1/5, (c) Cu/Co = 1/2, (d) Cu/Co = 2/1, and (e) Cu/Co = 5/1.

Table 2 Cu/Co ratio at the surface and in the bulk for the bimetal Cu@(CuCo-alloy)/Al_2O_3 catalysts

	Molar Cu/Co ratio	
Nominal ratio	Bulk (ICP)	Surface (XPS)
Cu/Co (5/1)	4.81/1.00	2.88/1.00
Cu/Co (2/1)	1.96/1.00	2.07/1.00
Cu/Co (1/2)	1.00/2.63	1.00/2.86
Cu/Co (1/5)	1.00/4.76	1.00/5.02

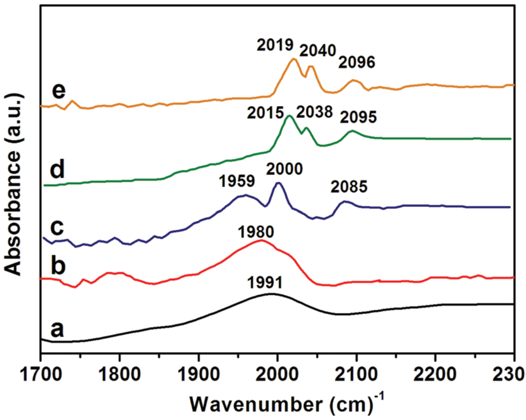

Fig. 11 *In situ* FTIR spectra of CO adsorption on (a) Co/Al_2O_3, and Cu@(CuCo-alloy)/Al_2O_3 samples with various Cu/Co ratios: (b) Cu/Co = 1/5, (c) Cu/Co = 1/2, (d) Cu/Co = 2/1, and (e) Cu/Co = 5/1.

band at 2015 cm^{-1} can be ascribed to coordinatively unsaturated Co^0 sites such as those located in steps or corners, while the contribution at 2038 cm^{-1} can be attributed to Co^0 sites located in planar (terrace) positions.[31] In addition, the IR spectra of CO adsorbed on Cu/Co (1/2), Cu/Co (2/1), and Cu/Co (5/1) samples (Fig. 11, curves c, d, e) show an absorption band at 2085, 2095 and 2096 cm^{-1}, respectively, accompanied by a gradually enhancing intensity, which points to the Cu^0 surface site.[32] In addition, this peak shifts to higher frequencies (from 2085 to 2096 cm^{-1}) along with an increase of the Cu content, further indicating the electron transfer from surface Cu species to Co species. It can be seen from Fig. 11 that the CO adsorption state on Co^0 species gradually transfers from bridge-type to linear-type along with the increase of the Cu content, which can be ascribed to the "active-site isolation" effect[33] imposed by Cu and thus a close interaction between Cu^0 and Co^0 species.

Previous researchers have concluded that the linearly adsorbed CO is the active site for the formation of oxygenated compounds, while the bridge-type adsorbed CO leads to the formation of hydrocarbon compounds, since the latter has a weaker C–O bond and thus can be more easily hydrogenated.[29b,34] The catalytic evaluation results (Table 1) show that the Co-rich catalysts (Co/Al_2O_3, Cu/Co (1/5) with dominated bridge-type adsorption) are more selective toward hydrocarbons, while the Cu-rich catalysts (Cu/Co (2/1), Cu/Co (5/1) with dominated linear-type adsorption) are prone to obtain oxygenated compounds. According to the reaction pathway for CO hydrogenation over the CuCo-based catalysts (Fig. S9†),[1a,3,7] Cu is the major element for methanol synthesis serving in the associative adsorption of CO, while Co affords the active site of the FT function of dissociative CO adsorption and hydrogenation. A synergistic effect between these two metal compositions is believed to be essential in this reaction. For the Cu@(CuCo-alloy)/Al_2O_3 (Cu/Co = 1/2) catalyst, copper species provides the active site for the associative adsorption of CO to produce CO*, while cobalt species acts as the active site for CO dissociation, C–C chain growth and hydrogenation to form the $*C_nH_z$ group. The CO* moves to the $*C_nH_z$ group and inserts *via* surface migration over a short distance between Co and Cu site for subsequent hydrogenation to produce higher alcohols.[3,7] A homogeneous distribution of copper and cobalt as well as their distance (geometric properties) are necessary to obtain higher alcohols. For the electronic interaction between Cu and Co, the electron transfer from Cu to Co increases the electron density of Co, which weakens the C–O bond of the adsorbed CO and facilitates its dissociation, while the decreased electron density of Cu enhances the associative adsorption of CO.[35] Therefore, both the geometric effect and electronic effect between Co and Cu contribute to the enhancement of selectivity toward higher alcohols.

4. Conclusions

In summary, a structured core–shell Cu@(CuCo-alloy)/Al_2O_3 catalyst was fabricated *via* a facile two-step procedure, the direct growth of CuCoAl-LDH nanoplatelets on aluminum substrates followed by a calcination–reduction process, and it serves as an efficient catalyst toward the CO hydrogenation (CO conversion: 21.5%; C_{6+} slate 1-alcohol selectivity: 48.9%). The specific core–shell structure Cu@(CuCo-alloy) NPs possess a Cu-rich core and a CuCo-alloy shell, which improves the electronic/geometric interaction between Cu and Co and effectively avoids phase separation during the catalytic reaction. In addition, the open channels associated with the hierarchical structure facilitate the mass diffusion/transport as well as inhibit the formation of hotspots. This strategy can be extended to synthesize other bimetallic catalysts derived from LDHs and offers new opportunities for achieving largely enhanced catalytic performances based on the bimetal synergistic effect.

Acknowledgements

This work was supported by the 973 Program (Grant no. 2011CBA00504), the National Natural Science Foundation of China (NSFC), the Beijing Natural Science Foundation (2132043), the Research on the Chemical Industry Cluster and the Socioeconomic Coordinated Development of Xinjiang (Grant no. JX20140015). M. Wei particularly appreciates the financial aid from the China National Funds for Distinguished Young Scientists of the NSFC.

Notes and references

1 (*a*) J. J. Spivey and A. Egbebi, *Chem. Soc. Rev.*, 2007, **36**, 1514; (*b*) V. Subramani and S. K. Gangwal, *Energy Fuels*, 2008, **22**, 814; (*c*) M. Behrens, F. Studt, I. Kasatkin, S. Kuhl, M. Havecker, F. Abild-Pedersen, S. Zander, F. Girgsdies, P. Kurr, B. L. Kniep, M. Tovar, R. W. Fischer, J. K. Norskov and R. Schlogl, *Science*, 2012, **336**, 893; (*d*) S. Zander, E. L. Kunkes, M. E. Schuster, J. Schumann, G. Weinberg, D. Teschner, N. Jacobsen, R. Schlogl and M. Behrens, *Angew. Chem., Int. Ed.*, 2013, **52**, 6536; (*e*) N. Yan, C. Zhao, C. Luo, P. J. Dyson, H. Liu and Y. Kou, *J. Am. Chem. Soc.*, 2006, **128**, 8714.

2 (*a*) M. Gupta, M. L. Smith and J. J. Spivey, *ACS Catal.*, 2011, **1**, 641; (*b*) M. R. Morrill, N. T. Thao, H. Shou, R. J. Davis, D. G. Barton, D. Ferrari, P. K. Agrawal and C. W. Jones, *ACS Catal.*, 2013, **3**, 1665; (*c*) J. Wang, P. A. Chernavskii, A. Y. Khodakov and Y. Wang, *J. Catal.*, 2012, **286**, 51; (*d*) V. R. Calderone, N. R. Shiju, D. C. Ferre and G. Rothenberg, *Green Chem.*, 2011, **13**, 1950.

3 K. Fang, D. Li, M. Lin, M. Xiang, W. Wei and Y. Sun, *Catal. Today*, 2009, **147**, 133.

4 (*a*) N. D. Subramanian, G. Balaji, C. S. S. R. Kumar and J. J. Spivey, *Catal. Today*, 2009, **147**, 100; (*b*) J. Wang, P. A. Chernavskii, Y. Wang and A. Y. Khodakov, *Fuel*, 2013, **103**, 1111; (*c*) W. Gao, Y. Zhao, J. Liu, Q. Huang, S. He, C. Li, J. Zhao and M. Wei, *Catal. Sci. Technol.*, 2013, **3**, 1324.

5 (*a*) X. Peng, Q. Pan and G. L. Rempel, *Chem. Soc. Rev.*, 2008, **37**, 1619; (*b*) F. F. Tao, S. Zhang, L. Nguyen and X. Zhang, *Chem. Soc. Rev.*, 2012, **41**, 7980; (*c*) T. Deng and H. Liu, *Green Chem.*, 2013, **15**, 116.

6 H. Wang, W. Zhou, J. X. Liu, R. Si, G. Sun, M. Q. Zhong, H. Y. Su, H. B. Zhao, J. A. Rodriguez, S. J. Pennycook, J. C. Idrobo, W. X. Li, Y. Kou and D. Ma, *J. Am. Chem. Soc.*, 2013, **135**, 4149.

7 G. Prieto, S. Beijer, M. L. Smith, M. He, Y. Au, Z. Wang, D. A. Bruce, K. P. de Jong, J. J. Spivey and P. E. de Jongh, *Angew. Chem., Int. Ed.*, 2014, **53**, 6397.

8 K. Xiao, X. Qi, Z. Bao, X. Wang, L. Zhong, K. Fang, M. Lin and Y. Sun, *Catal. Sci. Technol.*, 2013, **3**, 1591.

9 (*a*) X. Du, D. Zhang, L. Shi, R. Gao and J. Zhang, *Nanoscale*, 2013, **5**, 2659; (*b*) V. C. Deborah, A. P. Carlos, M. M. S. Vera and S. Martin, *Appl. Catal., A*, 1999, **176**, 205.

10 (*a*) G. R. Williams and D. O'Hare, *J. Mater. Chem.*, 1996, **16**, 3065; (*b*) A. M. Fogg, A. L. Rohl, G. M. Parkinson and D. O'Hare, *Chem. Mater.*, 1999, **11**, 1194; (*c*) L. Li, Y. Feng, Y. Li, W. Zhao and J. Shi, *Angew. Chem., Int. Ed.*, 2009, **48**, 5888; (*d*) S. He, S. Zhang, J. Lu, Y. Zhao, J. Ma, M. Wei, D. G. Evans and X. Duan, *Chem. Commun.*, 2011, **47**, 10797.

11 (*a*) A. Ota, E. L. Kunkes, I. Kasatkin, E. Groppo, D. Ferri, B. Poceiro, Y. R. M. Navarro and M. Behrens, *J. Catal.*, 2012, **293**, 27; (*b*) M.-Q. Zhao, Q. Zhang, X. L. Jia, J. Q. Huang, Y. H. Zhang and F. Wei, *Adv. Funct. Mater.*, 2010, **20**, 677; (*c*) M. Q. Zhao, Q. Zhang, J. Q. Huang and F. Wei, *Adv. Funct. Mater.*, 2012, **22**, 675.

12 (*a*) S. Xia, R. Nie, X. Lu, L. Wang, P. Chen and Z. Hou, *J. Catal.*, 2012, **296**, 1; (*b*) M. Behrens, I. Kasatkin, S. Kühl and G. Weinberg, *Chem. Mater.*, 2010, **22**, 386; (*c*) S. Y. Zhang, G. L. Fan and F. Li, *Green Chem.*, 2013, **15**, 2389; (*d*) H. Liu and E. Min, *Green Chem.*, 2006, **8**, 657.

13 (*a*) M. Q. Zhao, Q. Zhang, W. Zhang, J. Q. Huang, Y. Zhang, D. S. Su and F. Wei, *J. Am. Chem. Soc.*, 2010, **132**, 14739; (*b*) S. He, Z. An, M. Wei, D. G. Evans and X. Duan, *Chem. Commun.*, 2013, **49**, 5912; (*c*) S. He, C. Li, H. Chen, D. Su, B. Zhang, X. Cao, B. Wang, M. Wei, D. G. Evans and X. Duan, *Chem. Mater.*, 2013, **25**, 1040; (*d*) W. Gao, C. Li, H. Chen, M. Wu, S. He, M. Wei, D. G. Evans and X. Duan, *Green Chem.*, 2014, **16**, 1560.

14 (*a*) J. Liu, Y. Li, X. Huang, G. Li and Z. Li, *Adv. Funct. Mater.*, 2008, **18**, 1448; (*b*) H. Chen, F. Zhang, S. Fu and X. Duan, *Adv. Mater.*, 2006, **18**, 3089.

15 (*a*) G. Moretti, *J. Electron Spectrosc. Relat. Phenom.*, 1998, **95**, 95; (*b*) G. Moretti, *Surf. Sci.*, 2013, **618**, 3.

16 Z. Sun, L. Jin, S. He, Y. Zhao, M. Wei, D. G. Evans and X. Duan, *Green Chem.*, 2012, **14**, 1909.

17 (*a*) Y. Xiang, V. Chitry, P. Liddicoat, P. Felfer, J. Cairney, S. Ringer and N. Kruse, *J. Am. Chem. Soc.*, 2013, **135**, 7114; (*b*) C. N. Avila-Neto, D. Zanchet, C. E. Hori, R. U. Ribeiro and J. M. C. Bueno, *J. Catal.*, 2013, **307**, 222.

18 N. Barrabes, D. Cornado, K. Foettinger, A. Dafinov, J. Llorca, F. Medina and G. Rupprechter, *J. Catal.*, 2009, **263**, 239.

19 (*a*) Y. Song, H. Modrow, L. L. Henry, C. K. Saw, E. E. Doomes, V. Palshin, J. Hormes and C. S. S. R. Kumar, *Chem. Mater.*, 2006, **18**, 2817; (*b*) G. Ennas, A. Falqui, G. Paschina and G. Marongiu, *Chem. Mater.*, 2005, **17**, 6486; (*c*) X. Xie, Y. Li, Z. Q. Liu, M. Haruta and W. Shen, *Nature*, 2009, **458**, 746.

20 C. Philipp, D. D. Courty, F. Edouard and S. Andre, *J. Mol. Catal.*, 1982, **17**, 241.

21 (*a*) S. Wang, Y. Zhang and H. Liu, *Chem. – Eur. J.*, 2010, **5**, 1100; (*b*) W. Tong, A. West, K. Cheung, K. M. Yu and S. C. E. Tsang, *ACS Catal.*, 2013, **3**, 1231.

22 (*a*) A. M. Karim, Y. Su, M. H. Engelhard, D. L. King and Y. Wang, *ACS Catal.*, 2011, **1**, 279; (*b*) J. L. Ewbank, L. Kovarik, C. C. Kenvin and C. Sievers, *Green Chem.*, 2014, **16**, 885.

23 C. N. Ávila-Neto, D. Zanchet, C. E. Hori, R. U. Ribeiro and J. M. C. Bueno, *J. Catal.*, 2013, **307**, 222.

24 B. Bridier and J. Perez-Ramirez, *J. Am. Chem. Soc.*, 2010, **132**, 4321.

25 (*a*) J. P. Espinós, J. Morales, A. Barranco, A. Caballero, J. P. Holgado and A. R. González-Elipe, *J. Phys. Chem. B*, 2002, **106**, 6921; (*b*) M. C. Biesinger, L. W. M. Lau, A. R. Gerson, R. St. and C. Smart, *Appl. Surf. Sci.*, 2010, **257**, 887.

26 (*a*) J. Gong, H. Yue, Y. Zhao, S. Zhao, L. Zhao, J. Lv, S. Wang and X. Ma, *J. Am. Chem. Soc.*, 2012, **134**, 13922; (*b*) K. M. Yu, W. Tong, A. West, K. Cheung, T. Li, G. Smith, Y. Guo and S. C. Tsang, *Nat. Commun.*, 2012, **3**, 1230.

27 B. Bayram, I. I. Soykal, D. von Deak, J. T. Miller and U. S. Ozkan, *J. Catal.*, 2011, **284**, 77.

28 (*a*) A. Sharma, S. Tripathi and T. Shripathi, *Appl. Surf. Sci.*, 2009, **256**, 530; (*b*) J. Zhao, L. K. Ballast, T. Z. Hossain, R. E. Trostel1 and W. C. Bridgman, *J. Vac. Sci. Technol., A*, 2000, **18**, 1690.

29 (*a*) A. Yin, C. Wen, X. Guo, W. L. Dai and K. Fan, *J. Catal.*, 2011, **280**, 77; (*b*) F. Morales, E. Desmit, F. Degroot, T. Visser and B. Weckhuysen, *J. Catal.*, 2007, **246**, 91.

30 A. Y. Khodakov, J. Lynch, D. Bazin, B. Rebours, N. Zanier, B. Moisson and P. Chaumette, *J. Catal.*, 1997, **168**, 16.

31 G. Prieto, P. Concepción, R. Murciano and A. Martínez, *J. Catal.*, 2013, **302**, 37.

32 A. G. Sato, D. P. Volanti, D. M. Meira, S. Damyanova, E. Longo and J. M. C. Bueno, *J. Catal.*, 2013, **307**, 1.

33 (*a*) Y. Somanoto and W. M. H. Sachtler, *J. Catal.*, 1974, **32**, 315; (*b*) Y. He, L. Liang, Y. Liu, J. Feng, C. Ma and D. Li, *J. Catal.*, 2014, **309**, 166.

34 (*a*) N. Kumar, M. L. Smith and J. J. Spivey, *J. Catal.*, 2012, **289**, 218; (*b*) N. Tsubaki, *J. Catal.*, 2001, **199**, 236; (*c*) H. Xiong, Y. Zhang, K. Liew and J. Li, *J. Mol. Catal. A: Chem.*, 2008, **295**, 68.

35 (*a*) B. Qiao, A. Wang, X. Yang, L. F. Allard, Z. Jiang, Y. Cui, J. Liu, J. Li and T. Zhang, *Nat. Chem.*, 2011, **3**, 634; (*b*) R. Ramamoorthy and R. D. Gonzalez, *J. Catal.*, 1979, **58**, 188; (*c*) Y. Zhao, S. Li and Y. Sun, *J. Phys. Chem. C*, 2013, **117**, 24920; (*d*) V. Schwartz, A. Campos, A. Egbebi, J. J. Spivey and S. H. Overbury, *ACS Catal.*, 2011, **1**, 1298.